Failure Analysis of Three Si_3N_4 Balls Used in Hybrid Bearings

15 February 2003

Prepared by

M. J. O'BRIEN,[1] N. PRESSER,[2] and E. Y. ROBINSON[3]
[1]Space Materials Laboratory
[2]Electronics and Photonics Laboratory
Laboratory Operations
[3]Government Operations
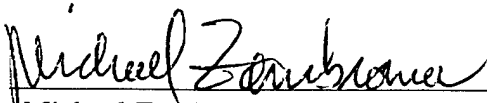Civil & Commercial Division

Prepared for

SPACE AND MISSILE SYSTEMS CENTER
AIR FORCE SPACE COMMAND
2430 E. El Segundo Boulevard
Los Angeles Air Force Base, CA 90245

Engineering and Technology Group

THE AEROSPACE CORPORATION
El Segundo, California

20030402 035

Michael Zambrana
SMC/AXE

REPORT DOCUMENTATION PAGE

1. REPORT DATE *(DD-MM-YYYY)* 15-02-2003	2. REPORT TYPE	3. DATES COVERED *(From - To)*

4. TITLE AND SUBTITLE	5a. CONTRACT NUMBER F04701-00-C-0009
Failure Analysis of Three Si$_3$N$_4$ Balls Used in Hybrid Bearings	5b. GRANT NUMBER
	5c. PROGRAM ELEMENT NUMBER

6. AUTHOR(S)	5d. PROJECT NUMBER
M. J. O'Brien, N. Presser, and E. Y. Robinson	5e. TASK NUMBER
	5f. WORK UNIT NUMBER

7. PERFORMING ORGANIZATION NAME(S) AND ADDRESS(ES)	8. PERFORMING ORGANIZATION REPORT NUMBER
The Aerospace Corporation Laboratory Operations El Segundo, CA 90245-4691	TR-2003(8565)-1

9. SPONSORING / MONITORING AGENCY NAME(S) AND ADDRESS(ES)	10. SPONSOR/MONITOR'S ACRONYM(S) SMC
Space and Missile Systems Center Air Force Space Command 2450 E. El Segundo Blvd. Los Angeles Air Force Base, CA 90245	11. SPONSOR/MONITOR'S REPORT NUMBER(S) SMC-TR-03-12

12. DISTRIBUTION/AVAILABILITY STATEMENT

Approved for public release; distribution unlimited.

13. SUPPLEMENTARY NOTES

14. ABSTRACT

The rolling-element fatigue life of advanced hybrid material bearings consisting of silicon-nitride balls, REX20 tool-steel inner races, and CRU20 tool-steel outer races was measured under well-qualified laboratory testing. Multiple sets of four bearings (207H size) were tested using the least-of-four technique and sudden-death statistics to obtain a Weibull distribution based upon a bivariate model that accounted for load, time, and sample size. The Weibull distribution model shows that the advanced material bearings are projected to have 6.7 times greater life than the reference 52100 steel bearings at 90% confidence and 12 times greater life at 50% confidence under the test conditions.

A fractographic analysis of three failed ceramic balls was performed. In each instance, the initiation of the final fracture was traced back to a relatively small site. In two cases, interesting features are identified that may represent the potential cause for the failure. These potential causes are identified as small defects that are believed to be sintering voids with diameters of less than 2 μm. The balls' very long lives under elevated loading suggest that the manufacturer is controlling the population of pre-existing manufacturing flaws very well.

15. SUBJECT TERMS

Bearing failures, Failure analysis, Fatigue design, Silicon-nitride hybrid bearings, Sintering voids

16. SECURITY CLASSIFICATION OF:			17. LIMITATION OF ABSTRACT	18. NUMBER OF PAGES	19a. NAME OF RESPONSIBLE PERSON Michael O'Brien
a. REPORT UNCLASSIFIED	b. ABSTRACT UNCLASSIFIED	c. THIS PAGE UNCLASSIFIED		24	19b. TELEPHONE NUMBER *(include area code)* (310)336-2878

**This Page Intentionaly
Left Blank**

Acknowledgments

**This Page Intentionaly
Left Blank**

Contents

Figures

Tables

1. Introduction

Over the last decade, silicon-nitride (Si_3N_4) balls have become an important component of advanced bearings used in a wide range of applications. The greatest commercial success for Si_3N_4 balls has been in "hybrid bearings" that combine the ceramic balls with steel races and are known as silicon-nitride hybrid bearings (SNHBs). Compared to the steel balls they replace, the ceramic balls are harder and less dense and offer higher compressive strength, better corrosion resistance, elevated operating temperature and reduced lubrication needs.[1] These benefits make the hybrid bearings ideal for severe high-speed applications such as machine tool spindles, dental drills, vacuum turbomolecular pumps, and the liquid-oxygen turbomolecular pumps used in the Space Shuttle main engines.[2]

However, information on the fatigue life of these hybrid bearings is limited, and data on scaling effects for various operating loads and for various size bearings are very sparse. Accordingly, a test program was undertaken to measure and compare the life of SNHBs relative to reference 52100 steel bearings under well-qualified laboratory rolling-element fatigue testing in which the load, speed, lubrication, and lubricant temperature were very carefully controlled. A Weibull statistical analysis of the test data is presented that suggests much greater life for the hybrid bearings than for the reference all-steel bearings.

In this paper, we present a fractographic analysis of Si_3N_4 balls from hybrid bearings that failed during the testing. The fractography was performed with a field-emission scanning electron microscope operated at such a low voltage that the actual surface could be examined without the need for a conductive coating.[3] A thin, conductive coating (such as carbon or gold) is otherwise ordinarily needed at higher operating voltages to prevent charging on the Si_3N_4, which is an electrical insulator.

A recent review article surveys the topic of fractography of ceramics.[4] An early fractographic analysis identified gross processing defects in hot pressed Si_3N_4 bearings whose fractures displayed characteristic Wallner lines centered on the defects.[5] Fractography has also been used to relate defect size to strength in sintered Si_3N_4[6] and to identify the micromechanics of cyclic fatigue in monolithic Si_3N_4.[7,8] A worldwide consortium of research agencies has sponsored a round-robin evaluation of various fractured ceramics to the standards of the U.S. Department of Defense's Military Handbook 790, "Fractography and Characterization of Fracture Origins in Advanced Structural Ceramics."[9]

2. Experimental Procedure

2.1　Rolling-Element Fatigue Testing

A test series was undertaken to demonstrate the rolling-element fatigue life of advanced material bearings consisting of Si_3N_4 balls, REX20 inner steel races, and CRU20 outer races.[10,11] To provide a baseline reference, industry-standard steel bearings with 52100 steel balls and 52100 steel races were also tested.

These advanced material bearings are called "hybrid" bearings because they combine both steel and ceramic components. The Si_3N_4 balls were MgO doped, hot isostatically pressed, and lapped to AFBMA* Grade 3 surface finish and dimensional control. REX20 is an air-melted powder metallurgy version of M62 tool steel, and CRU20 is, in turn, the vacuum induction-melted version of REX20. The REX20/CRU20 steels were quenched and triple tempered to achieve a hardness of HRC 66-67 with a retained austenite of less than 5 vol% as measured by X-ray diffraction.[10,11] The bearings were the 207H size, which is a standard catalog bearing. The type 207H bearing has an outer diameter of 72.0 mm, an inner bore diameter of 35.0 mm, an external width of 17.0 mm, and a ball diameter of 11.906 mm (15/32 in.).

Fatigue testing was performed on full-scale bearings using a standard bearing test fixture. All bearings were thrust loaded, rotated at 565.5 rad/s (5400 rpm), and lubricated with a continuous flow of MIL-L-7808 oil at 0.95 L/min/bearing. The oil was maintained at a temperature of 71°C and filtered to the 3-μm level. These conditions resulted in $\lambda = 1$, where λ is the ratio of the calculated lubricant film thickness divided by the average of the surface roughness. The test system was monitored and capable of detecting a spall as small as 3 mm in diameter, at which point the test was suspended.

Test protocol was sudden-death statistics with six test groups of four bearings in each group using the least-of-four technique to obtain a Weibull distribution. Under this protocol, the first failure in each group of four bearings suspended the test of the other three bearings, resulting in an estimate of the life, as explained below. The test period for the first phase of testing was 2600 h, at which time testing was suspended even if no bearings had failed.

It was originally planned to test the different material bearings under equivalent Hertzian contact stresses. The standard 52100 bearings were tested under an axial thrust load of 13,300 N (3000 lbf), which gave a mean Hertzian stress of 1.88 GPa (273 ksi). To provide equivalent Hertzian stress, the hybrid bearings were initially tested under an axial load of 6,650 N (1500 lbf), which gave the same mean Hertzian stress of 1.88 GPa due to the higher elastic moduli of REX20 and Si_3N_4. As explained below in the results section, all of the 52100 steel bearing test groups failed before the maximum tar-

---

* Anti-Friction Bearing Manufacturers Association, NY, NY.

3

get life of 2600 h was reached. In contrast, none of the hybrid bearings failed in the initial testing before the maximum target life was reached.

Consequently, to learn how they perform at equivalent axial loads, the hybrid bearings were tested at an axial load of 13,300 N, which was the same load used for the reference 52100 bearings. The Hertzian stresses are substantially higher for these hybrid bearings (2.29 GPa) than for the 52100 steel bearings (1.88 GPa) under this identical axial load of 13,300 N. Due to the limited availability of REX20 races, only four sets of four bearings were tested under this condition of equivalent axial load. The lifetimes for the first and second phases of testing are given below in the results section.

2.2 Electron Fractography

After testing was completed, a scanning electron microscope (SEM) was used to conduct a fractographic examination of the failed Si_3N_4 balls to identify the microstructural feature responsible for their failure. The SEM* used a cold-field emission electron source with tungsten single-crystal tip. The sample chamber operated at a vacuum of 4×10^{-7} Torr. To prevent charging, a low accelerating voltage of 1 kV was used to image the bare ceramic. At such a low accelerating voltage, it was not necessary to coat the ceramic with any conducting layer, such as pyrolytic carbon or gold. A tip current of less than 6×10^{-12} A allowed images up to 30,000 times magnification at 1 kV without charging.

In general, the long-term cleanliness of the microscope's vacuum chamber is the critical limiting factor for high-resolution and high-magnification imaging of uncoated ceramic surfaces at low voltages. Careful sample preparation and handling prevent carbonaceous contamination of the vacuum, which minimizes inadvertent carbonaceous deposition by the electron beam onto the surface being examined. The carbonaceous deposits are undesirable because they obscure sample details at low voltage and because they are much more prone to charging than the bare ceramic.

---

*JEOL 6401-F

3. Results

3.1 Rolling-Element Fatigue Testing

To provide a reference, six groups of four 52100 steel bearings were tested at a mean Hertzian stress of 1.88 GPa. The times to first failure in each group of four were 17, 47, 127, 339, 364, and 910 h. In the first phase of testing, six groups of four hybrid bearings were also tested at an identical Hertzian stress of 1.88 GPa. All of these hybrid bearings, a total of 24, exceeded 2600 h of testing without a single failure. Specifically, the six tests ran for 2630, 2784, 2630, 2611, 2611, and 2611 h when testing was discontinued.

In the subsequent second phase of testing,* four groups of four hybrid bearings were tested at an elevated Hertzian stress of 2.29 GPa. For the four test groups, three bearings failed at 1548, 3408, and 3441 h due to a ball failure, and the fourth bearing failed at 2250 h due to the failure of the inner steel raceway. Our records identify which ball failed at 1548 h but did not indicate which of the two remaining failed balls failed at 3408 h and which failed at 3441 h. It should be noted that two of the four test groups were forced to run well past their target life of 2600 h before failure was reached.

3.2 Weibull Analysis

A detailed fatigue life treatment via a bivariate Weibull model for these and other silicon-nitride bearing data is documented elsewhere. A summary of the method, assumptions, and inferences is presented here. The bearing is treated as a single entity experiencing any fatigue failure mode, with fatigue life in hours of operation at 565.5 rad/s (5400 rpm) under constant load. The forecasts apply strictly to size 207H bearing as shown.

The issues to be addressed are:

1. Conversion of least-of-four probability data to single-bearing data;

2. Probability plotting positions for single bearings;

3. The load-life exponent connection to the shape parameters of a bivariate Weibull Distribution;

4. Weibull size effect for inferring single bearings median life from observed least-of-four median life;

5. Fatigue life distribution and design forecast equation and chart for 207H bearings.

---

* In the first phase of testing with 24 bearings, the outer races of the bearings were REX20 steel. In the second phase of testing of 16 bearings, the outer races were CRU20 steel, as explained above in Subsection 2.1.

3.2.1 Converting Least-of-Four Data to Single-Bearing Statistics

If the single bearing survival probability is S_1, then the probability of N bearings surviving is $S_N = S_1^N$. The single bearing failure probability, F_1, may be inferred from the observed least-of-N value as:

$$F_1 = 1 - (1 - F_N)^{1/N}.$$ (1)

In the present case $N = 4$, and

$$F_1 = 1 - (1 - F_4)^{1/4}.$$ (2)

3.2.2 Probability Plotting Position

The data are ranked by increasing order, with j the rank number (or, alternatively, the position in the order). The median rank plotting position, which is well proven as the most representative,[12] is used:

$$F_j = (j - 0.3)/(N + 0.4),$$ (3)

where F_j is the cumulative probability of failure, j is the rank number, and N is the total sample size. These are shown in Table 1. Equation (3) allows the ranking and plotting of failure probabilities for single bearings. The values in Table 1 are used below in Subsection 3.2.5 to plot the individual experimental data points from Subsection 3.1 on the failure probability chart shown in Figure 1.

Table 1. Probability Plotting Position Values for a Group of Four Bearings and a Single Bearing

j	F_j for a Group of 4 Bearings	F_j for a Single Bearing
1	0.159	0.042
2	0.386	0.115
3	0.614	0.212
4	0.841	0.368

3.2.3 The Load-Life Exponent

The seminal work of Lundberg and Palmgren[13,14] is based on Weibull's theory of statistical brittle fracture,[15,16] in a bivariate form, applied to fatigue life. This method has gained acceptance through much of the bearing industry for correlating rolling-element bearing fatigue life and establishing design levels. Lundberg and Palmgren utilize power-law assumptions for the variates of load (stress) and life, following the recommendations of Weibull. Application of the bivariate Weibull Distribution to static fatigue and development of design forecasts are given by Robinson,[17] which expands the method used here.
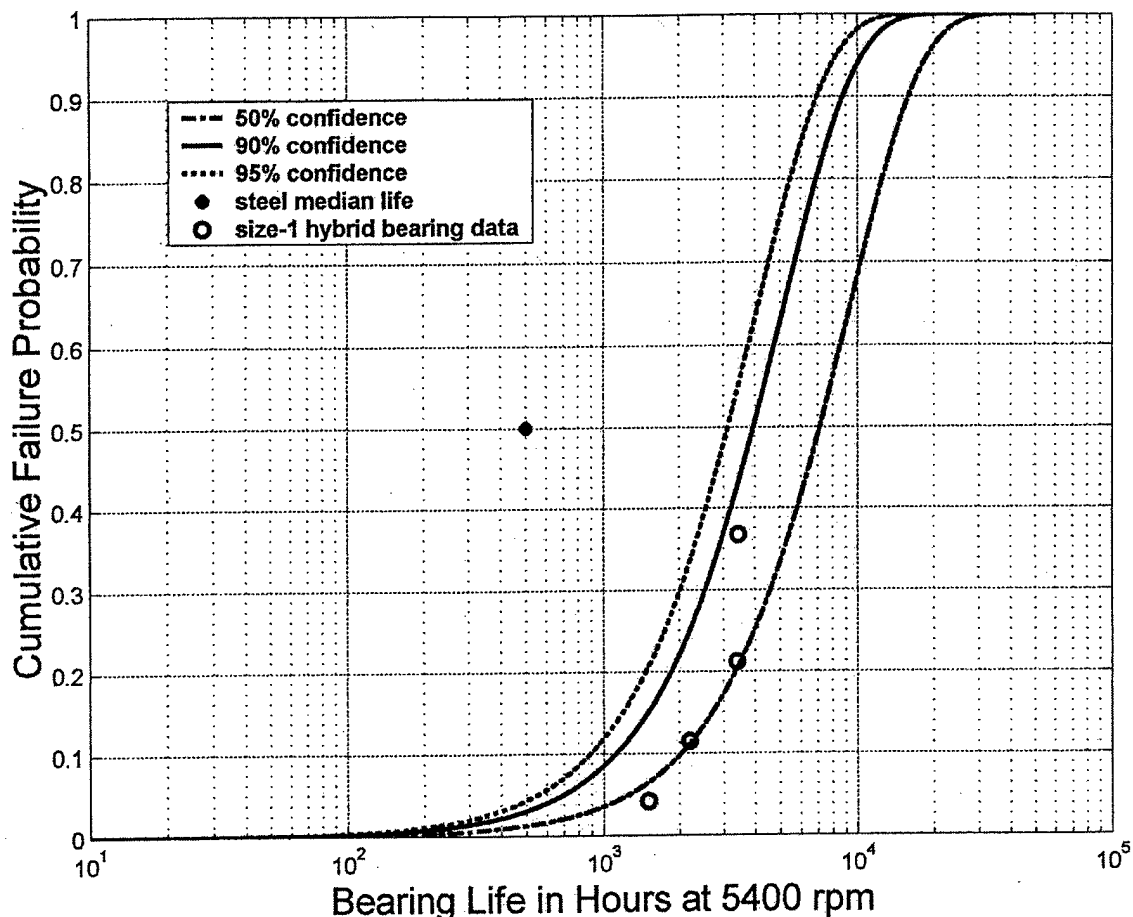
Figure 1. Projected fatigue life of type 207H silicon-nitride hybrid bearings at 13,300 N load and 5400 rpm shaft speed.

A bivariate Weibull Model accounts in a rational manner for the effect of load and time and leads to convenient design forecasts for the size 207H bearings tested in this program:

$$S = Exp[-KH^m T^e], \qquad (4)$$

where S is the cumulative survival probability, H is a scaled load normalized to the median strength, and T is the scaled lifetime, also conveniently normalized to median life. K is a constant that established the normalizing probability. The exponent m is the strength-shape factor (as used by Weibull), and e is the life-shape factor (as used by Lundberg and Palmgren and called the Weibull Slope).

For example, the median normalized form is given by:

$$Ln(1/S)/Ln(2) = (H/H_{50})^m (T/T_{50})^e. \qquad (5)$$

7

Or, the more general form, for any convenient percentile S_r (e.g., for censored datasets):

$$\text{Ln}(1/S)/\text{Ln}(1/S_r) = (H/H_r)^m (T/T_r)^e, \tag{6}$$

where r is the percentile. Here, a fixed load gives median normalized fatigue life, and, at constant life, the median normalized strength distribution results. Both distributions must be self-consistent.

At a fixed probability value,

$$H^m T^e = \text{constant}. \tag{7}$$

The load-life exponent, relating increased life with decreased load, is

$$H^{m/e} T = \text{constant}. \tag{8}$$

Or, equivalently,

$$(\text{Load})^{m/e} (\text{Life}) = \text{constant}. \tag{9}$$

This relationship connects the statistical strength distribution to fatigue life distribution. The load-life exponent, m/e, which is the ratio of shape factors, is the inverse ratio of strength scatter to life scatter. It is termed p by Lundberg and Palmgren. The selected Weibull slope, e, and the load life ratio, m/e, were estimated from a survey of the vast body of many thousands of bearing fatigue tests[13,18,19] with data for conventional bearings, along with much smaller datasets available for silicon-nitride bearings. The recommendations, consistent with Palmgren and Lundgren's assessments, lead to the following ground rules for this study:

$$e = 1.5 \tag{10}$$

and

$$m/e = 3. \tag{11}$$

The Weibull Modulus for strength is inferred from the load-life exponent. This means that the Weibull Modulus (slope) for strength corresponds to m = 4.5, a relatively low number for a brittle material. If the actual value for silicon nitride is higher, as expected, then the load-life exponent should be correspondingly higher, and the assumptions here are, therefore, undoubtedly conservative.

3.2.4 The Size Effect

The Weibull size effect is used to infer the fatigue life of single bearings (or, size-1 specimens) from the observed median life of groups of 4 bearings (or, size-4 specimens). The Weibull distribution form is given by:

$$S_1 = Exp[-(T_1)^e]$$ (12)

where S_1 is the cumulative survival probability of a size-1 specimen, e is the Weibull slope, and T_1 is the lifetime of the size-1 specimen.

And for the least survivor among a size-N specimen:

$$S_1 = e^N S_N = Exp[-N (T_N)^e],$$ (13)

where S_N is the survival probability of a size-4 specimen, T_N is the lifetime of the size-N specimen, and e in the preceding is the Weibull slope (not the operation of exponentiation).

At equal probabilities this leads to the well known Weibull size effect:

$$T_1 = (N)^{(1/e)} T_N .$$ (14)

By substitution into Eq. (13), it follows that

$$Size\text{-}1 \text{ life} = (4)^{1/1.5} * (Size\text{-}4 \text{ life}) .$$ (15)

From the experimental data, the observed size-4 failures are 1548, 2250, 3408, and 3441 h. Hence, the size-4 median life is (2250 h + 3408 h)/2 = 2829 h (at 5400 rpm). From Eq. (15), the size-1 median life is 2.52 x 2829 h = 7130 h or 2.3 x 10^9 shaft cycles.

For the size 207H bearing at constant load, the life distribution is given by:

$$S = Exp[-Ln(1/S_r)(T/T_r)^e] ,$$ (16)

where $S_r = 0.5$ and $t_r = 7130$ h from the preceding paragraph.

For conservative design forecast purposes, the central value is shifted to a higher confidence level by a K-factor derived from the central limit theorem. The coefficient of variation (CV) of the central value is given by the data's CV divided by the $\sqrt{N}$. The coefficient of variation is given for a Weibull

distribution to very close approximation by $(1/m)^{0.94}$, which gives 0.68/2 or 0.34 for m = 1.5 and N = 4. In addition, from Eq. (15), the single-bearing life is obtained by multiplying the size-4 bearing life by 2.52. After invoking this size effect factor, the median life at the 90% confidence level is obtained by shifting the central value by 1.31 standard deviations (that is, K = 1.31). More explicitly, the median life at the 90% confidence level is equal to the median life at the 50% confidence level multiplied by (1 – 1.31*0.34). Similarly, for the 95% confidence limit, the central value is shifted 1.65 standard deviations.

For the SNHB test data, Table 2 summarizes the K-factor and median lifetimes at 50%, 90%, and 95% confidence levels. Also shown is the ratio of median lifetimes for the SNHBs to the reference steel bearing median life of 587 h.

The distributions from Eq. (16) are plotted in Figure 1. The quantity plotted is the cumulative failure probability, which is, of course, equal to 1 – S. The distributions at the 50%, 90%, and 95% confidence levels are obtained by inserting the respective median lives of 7130, 3954, and 3130 h into T_R in Eq. (16). Also plotted in Figure 1 are the experimental data points for the steel and hybrid bearings. As mentioned above, the values from Table 1 allow the ranking and plotting of the hybrid bearing data.

Table 2.   SNHB Median Life at 50%, 90%, and 95% Confidence Levels and Comparison to Steel-Bearing Median Life

Confidence Level	K-Factor	SNHB Median Life	Ratio of SNHB Life to Steel-Bearing Median Life
50%	1.00	7130	12
90%	1.31	3954	6.7
95%	1.65	3130	5.3

3.2.5   Design Forecast Equation

The default values for Weibull slope and load-life exponent define a bivariate distribution, which modifies Eq. (16) and provides the following general equation for forecasting survival times at different applied loads based on a desired level of confidence:

$$S = Exp\ [-Ln(1/S_r)[(X/X_r)^m(T/T_r)^e]],\qquad(17)$$

where S is the desired survival probability contour, X is the applied load at which the life is forecast, T is the forecasted life, X_r is the applied load at which data were measured, T_r is the median life at a desired confidence, and S_r is the 50 % (median) survival percentile.

Rearranging and solving for the load at which the life is forecast gives the following:

$$Log(X) = (e/m)Log[T] + (e/m)Log[T_r] + Log[X_r] + Log[Ln[1/S]/Ln[1/S_r]],\qquad(18)$$

where m = 4.5 (from the assumed load-life exponent of 3), e = 1.5, T_r = 3954 h at 90% confidence (from Table 2), S_r =0.5 and X_r = 13,300 N.

Equation (18) is plotted in Figure 2, which shows survival contours for S = 0.5, 0.9, 0.99, 0.999, and 0.9999 at 90% confidence. Figure 2 is a design forecast chart for the type 207H silicon-nitride hybrid bearing that can be used to forecast the bearing load for different desired survival times at 90% confidence level at a bearing shaft speed of 5400 rpm.

3.3   Electron Fractography

A fractographic analysis of the three failed Si_3N_4 balls from the elevated stress testing of the hybrid bearings was performed to assign a cause for the failure. Each failure is discussed separately in the following sections. As an explanatory note, Wallner lines are curved and wavelike markings on the surface of fractured ceramic. The fracture origin is always on the concave side of the Wallner lines, which can be used to determine the origin and direction of propagation of the fracture.[20] As terminology, the fracture origin is "upstream" in the fracture and the fracture grows in the direction from the "upstream" location to the "downstream" location.
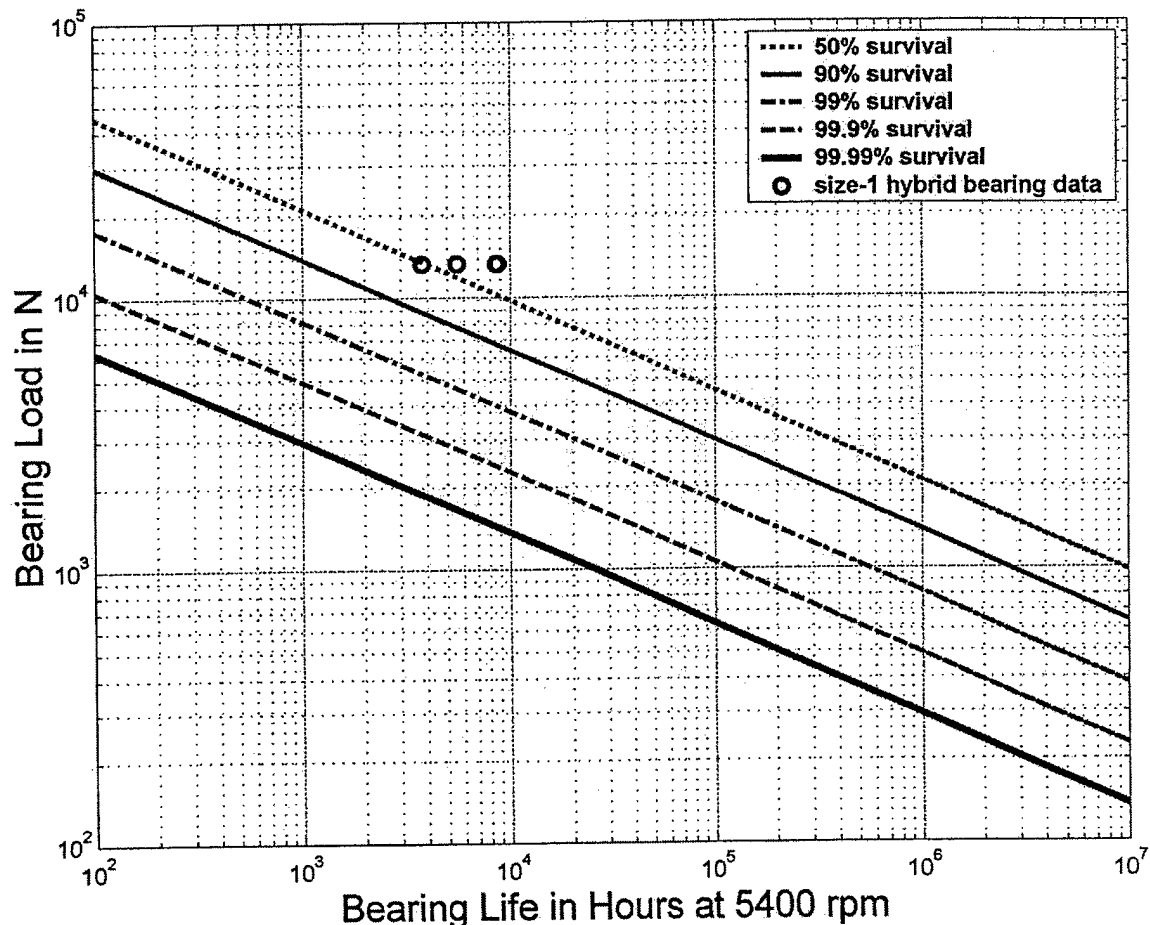

Figure 2.   Bivariate Weibull fatigue design model for type 207H silicon-nitride hybrid bearings at 5400 rpm shaft speed and 90% confidence level.

11

3.3.1 Fractographic Analysis of First Si₃N₄ Ball (1548 h of service until failure)

Figure 3 is a low-magnification view of the entire spall from a perspective perpendicular to the surface. The Wallner lines radiate on the left and right from an initiation site labeled "A," with the concave sides of the Wallner lines pointing back towards this initiation site, which is a broad, flat "plateau." Figure 4 is a more highly magnified view centered to the left-hand side of the initiation site "A," and Figure 5 is a companion view centered to the right-hand side. Figures 4 and 5 are taken at oblique angles to highlight the concave Wallner lines, which again are seen to point back towards the site "A," which is, therefore, identified as the initiation site.

Figures 6 is a more highly magnified view (at 100X) centered on the site "A" from an oblique perspective. The circular Wallner lines seen in site "A" form a "bull's eye" pattern around a central point, labeled "B." The pattern of Wallner lines implies that the site "B" is the upstream location where failure initiated. Detailed inspection of site "B" at still higher magnifications did not seem to reveal a clear cause for the initiation of the fracture.
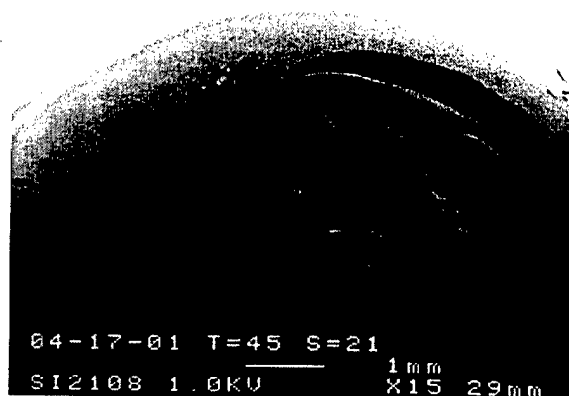

Figure 3. Low-magnification view of the entire spall.

Figure 4. View centered to the left-hand side of the initiation site "A."

Figure 5. Companion view centered to the right-hand side of the initiation site "A" (this view is upside down from the previous view).

Figure 6. View centered on the initiation site "A" showing a central "bull's eye" pattern of Wallner lines.

12

3.3.2 Fractographic Analysis of Second Si₃N₄ Ball (greater than 3400 h of service until failure)

Figure 7 is a low-magnification view of the entire spall. To orient the discussion of subsequent fractographs that show finer detail, five features are labeled in Figure 7. In this view, the circular Wallner lines are evident in the upper and left-hand parts of the spall. In particular, feature "A" is a region of Wallner lines in the middle of the spall. Feature "B" is a region of Wallner lines upstream from feature "A." The concave lines radiate back to a point labeled "C," which is a void in a triangular pocket defined by the intersection of three cracks. (In the following more highly magnified fractographs, feature "C" is shown to be a void). The long feature labeled "D" is a deep "trench-like" fracture. An interesting feature, labeled "E," is a patch of virgin surface that did not spall away.

Figures 8 and 9 are low-magnification views taken by successively rotating the line of sight. The concavity of the Wallner lines, labeled "A" and "B," again reinforces that fracture initiated in an upstream location in the neighborhood of the feature "C," from which radiates the deep fracture "D." Two other cracks, labeled "F" and "G," also radiate from the feature "C." To provide a landmark, the location of the unspalled virgin surface is labeled "E."

Figure 7. View of the entire spall.

Figure 8. View from an oblique perspective of Wallner lines downstream from the initiation site, "C."

Figure 9. View of from an orthogonal perspective Wallner lines downstream from the initiation site, "C."

Figures 10, 11, and 12 are progressively higher magnification views (at 25x, 180x and 3500x, respectively) from an orthogonal perspective and centered on the feature labeled "C," which is revealed to be a void in a triangular pocket at the junction of the three cracks, "D," "F," and "G." Figure 13 is a view of the void from a different perspective that "sights" down the bore of the void. The void, which is approximately 2 μm in diameter, may be a small sintering pore where the ceramic did not fully densify. Figure 14 is a micrograph at a slightly elevated accelerating voltage, 3 kV, that shows that the region immediately around the void charges, although material further away does not. The discussion section expands upon the possible significance of the observed charging.
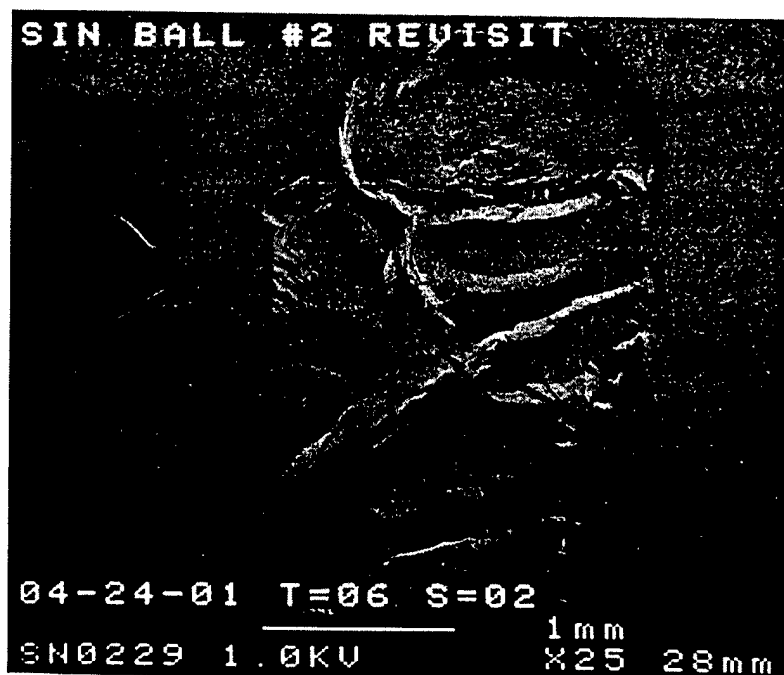

Figure 10.   First in a series of three views centered on the initiation site, "C," from which three cracks radiate.

Figure 11.   More highly magnified view centered on the initiation site, "C."

Figure 12.   Magnified view of void, from which fracture initiated, that displays a different fracture appearance at the void.
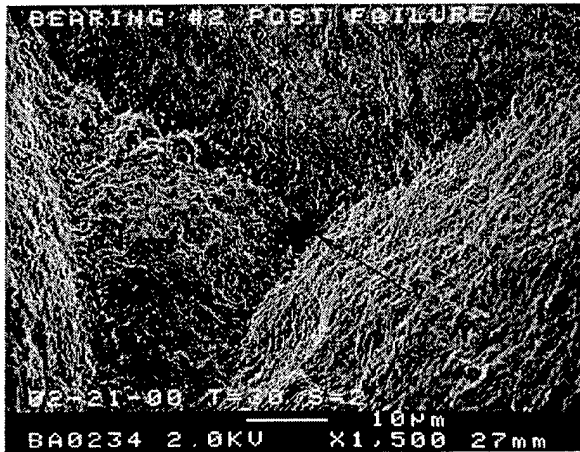
14

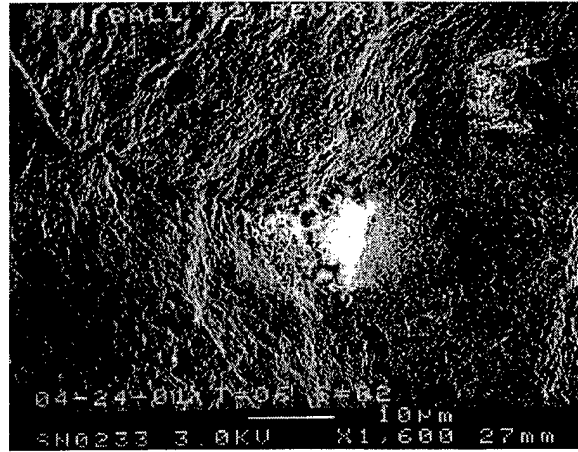Figure 13. View sighting down the bore of the void. (The orientation is rotated from the previous figures.)

Figure 14. The void and its vicinity display charging at a slightly elevated accelerating voltage of 3 kV.

3.3.3 Fractographic Analysis of Third Si_3N_4 Ball (greater than 3400 h of service until failure)

Figures 15 and 16 are low-magnification views of the entire spall. The origin of the failure appears to be a broad, flat "plateau." Circular Wallner lines radiate from the center of the plateau and down several "stepped" regions, with the concave sides of the Wallner lines pointing back towards the initiation site. The concavity reinforces the notion that the plateau is "upstream" in the fracture, and the several stepped regions are "downstream." Two features, "A" and "B," are labeled in the center of the plateau to provide landmarks, but are seen more clearly in the following more highly magnified fractographs.
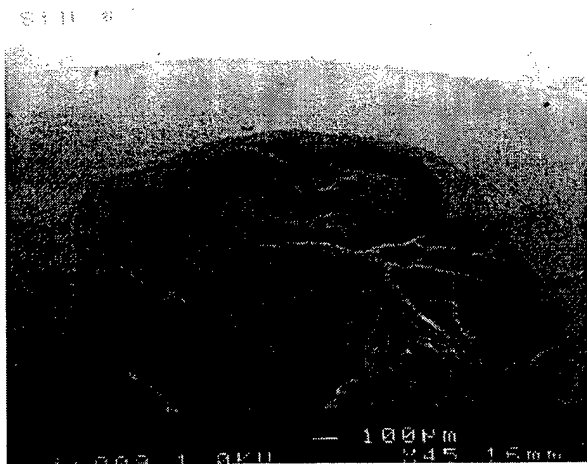

Figure 15. Low-magnification view of the entire spall showing Wallner lines radiating from a broad, flat "plateau."
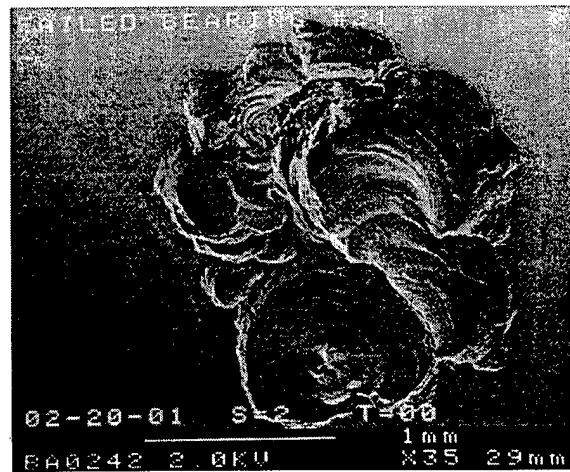

Figure 16. Another low-magnification view of the entire spall (the view is upside down from the previous figure).

15

Figure 17 is a more highly magnified view of the plateau from which fracture initiated. The Wallner lines form a "bull's eye" pattern around a central point. The "thumb-shaped" feature labeled "A" is a landmark used to orient subsequent discussion. Running off from point "A" is a crack-like feature labeled "B." Another landmark is labeled "D."

Figures 18 through 21 are progressively more highly magnified views (at 95x, 300x, 3500x, and 15,000x, respectively) of a separate crack-like feature, labeled "E," from an orthogonal perspective. Feature "E" is at the base of feature "A" near feature "D." Features "A," "B," and "D" are labeled in Figures 18 and 19 for orientation. The feature "E" is just inboard of the tightly spaced Wallner lines in the upper right-hand corner of Figure 19, which reinforces the notion that feature "E" is in the right location to be the site for fracture initiation. Figures 20 and 21 show an interesting structure in the crack-like feature "E." In the structure, ligaments span the crack-like feature. The discussion section expands upon the possible significance of the ligaments.
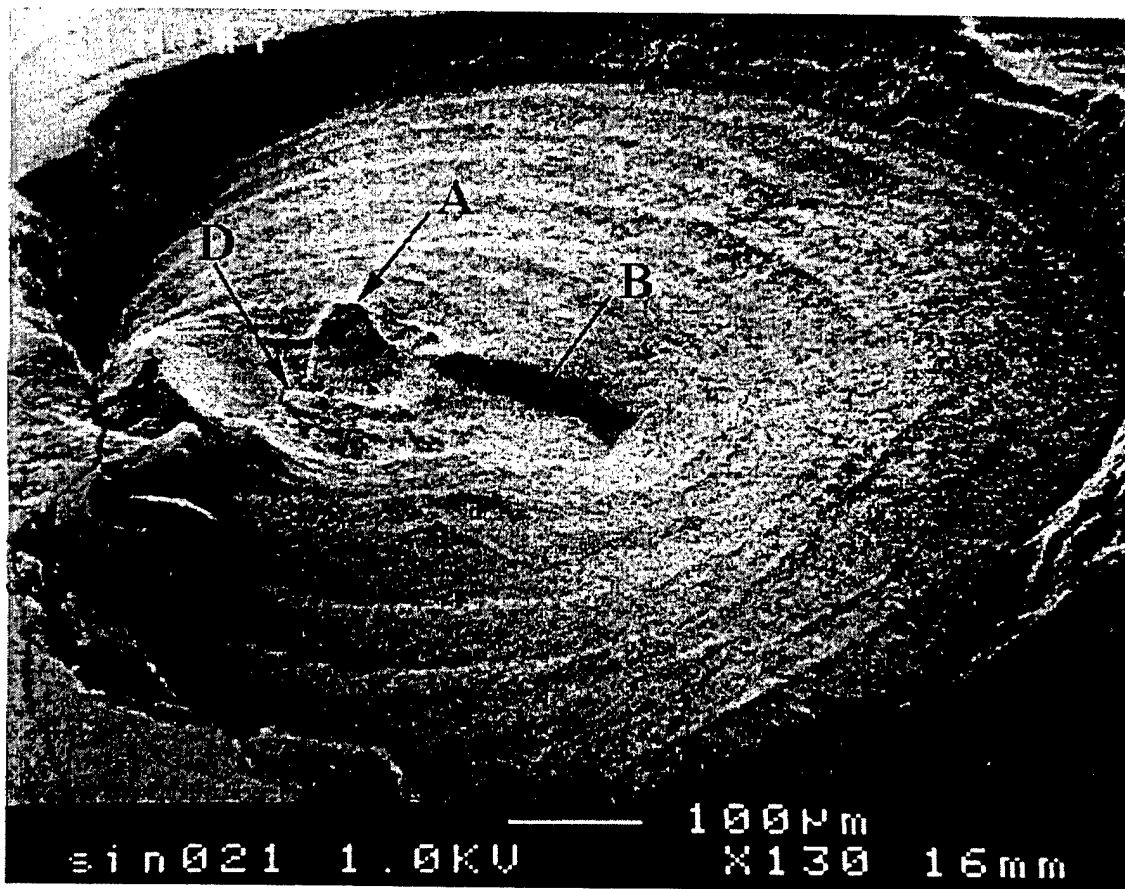
Figure 17.   View centered on the plateau from which fracture initiated. The
Wallner lines form a "bull's eye" around a center.

Figure 18. First in a series of four views centered on the initiation site.

Figure 19. More highly magnified view centered on the initiation site, "E," which is just inboard of the Wallner lines in the upper right-hand corner of the image.

Figure 20. Ligaments span crack-like feature at the initiation site, "E."

Figure 21. Highly magnified view of the string of ligaments, to which the arrows point.

4. Discussion

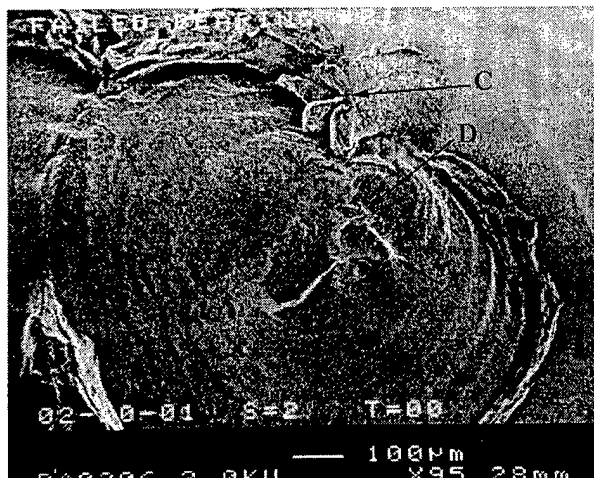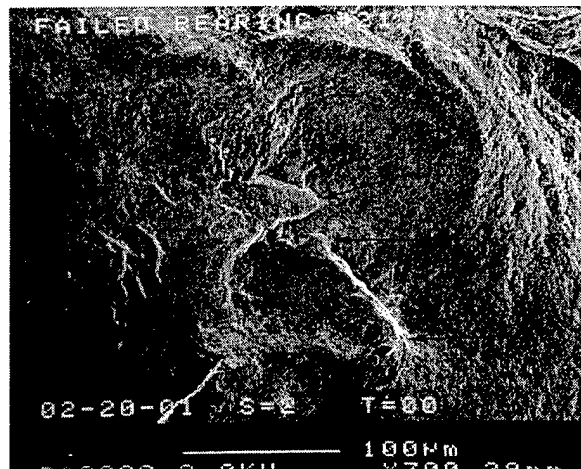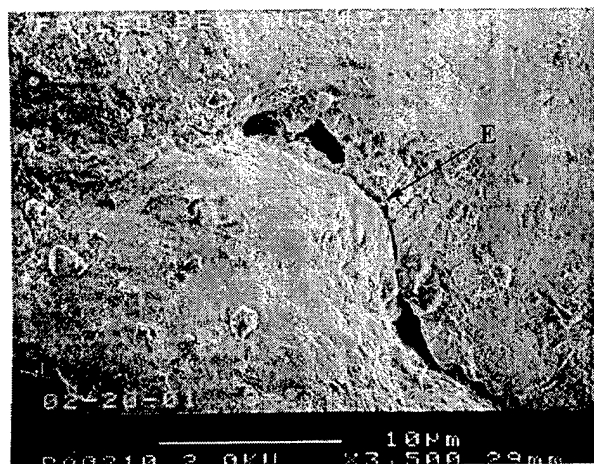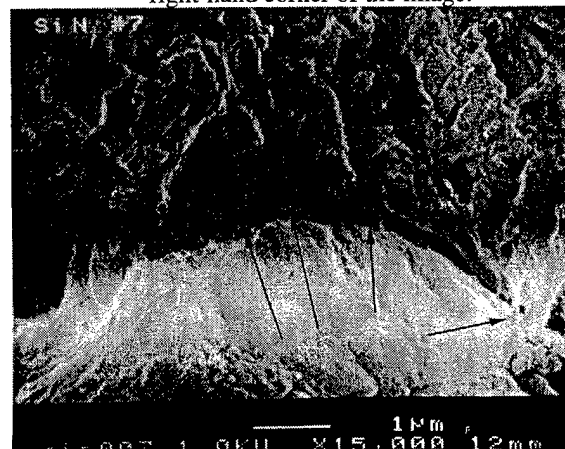The balls' very long lives under elevated loading suggest that the manufacturer is controlling the population of pre-existing manufacturing flaws very well. For two of the examined balls, the potential causes for the failures were identified as small defects that are believed to be sintering voids with diameters of less than 2 μm. The identified microstructural features may naturally represent the limit of defects that can be controlled through processing. It is possible that such small defects should be considered defects inherent to the material rather than manufacturing defects.

The fractographic analysis of the first Si_3N_4 ball in Subsection 3.3.1 identified the initiation site for the failure, but did not identify the microstructural feature responsible for the initiation. It is possible that the microstructural feature did not survive the failure.

The fractographic analysis of the second Si_3N_4 ball in Subsection 3.3.2 showed a small void that sits in a triangular region whose appearance differs from the fracture surface around it, which is seen most clearly in Figures 12. This change in appearance may imply that the triangular region is not the same chemistry as the material around it. For example, the region may be a pocket of segregated glassy material at the triple junction between adjacent grains of crystalline Si_3N_4. The observation that the triangular region charges implies that the region has a higher electrical resistivity than the material around it. A higher electrical resistivity might be consistent with a pocket of glassy material rich in the sintering aids used in this Si_3N_4. The glassy sintering aids might be expected to be more insulative than the bulk Si_3N_4 ceramic.

Alternatively, the change in appearance might imply that the triangular region possessed a different history than the material around it during the fracture process. For example, if the void does represent the initiation of the spall, then the region may be the site where a sub-critical pre-crack developed and slowly grew by fatigue over several million Hertzian loading cycles until it reached the critical size at which the rest of the spall fractured. During the course of the fatigue cycles, asperities may have been smoothed away as the opposing faces of the pre-crack opened and closed, giving the change in appearance compared to the larger fracture surface around it.

The fractographs of the third ball in Subsection 3.3.3 show an interesting feature in the crack-like feature "E," which can be seen in Figures 20 and 21. The ligaments spanning the crack-like feature have a distinctive elliptical shape that might be characteristic of the neck that forms during sintering and pore consolidation. The neck's elliptical shape might be interpreted as the negative radius of curvature that forms at the junction between two sintered particles. That is, the ligaments may be the remnants of a string of small sintering voids that did not fully densify. If so, then the ligaments might be expected to be glassy pockets rich in the liquid-phase sintering aids used in this ceramic. It is uncertain, however, whether the ligaments represented the initiation site for the fracture, whether the ligaments developed as damage late in the fracture, or whether the ligaments were unrelated to the fracture.

19

5. Conclusions

The rolling-element fatigue life of advanced material bearings consisting of silicon-nitride balls, REX20 tool-steel inner races, and CRU20 tool-steel outer races was measured in well-qualified testing with careful control of load, speed, and lubrication. Multiple sets of four bearings (207H size) were tested using the least-of-four technique and sudden-death statistics to obtain a Weibull distribution based upon a bivariate model that accounted for load, time, and sample size. The Weibull distribution showed that the advanced material bearings are projected to have 6.7 times greater life than conventional 52100 steel bearings at 90% confidence and 12 times greater life at 50% confidence. The balls' very long lives under elevated loading suggest that the manufacturer is controlling the population of pre-existing manufacturing flaws very well.

A fractographic analysis of three failed ceramic balls showed that the initiation of the final fracture could be traced back to a relatively small initiation site. In two cases, the initiation sites are identified as small defects that are believed to be sintering voids with diameters of less than 2 μm. The identified microstructural features may naturally represent the limit of defects that can be controlled through processing. It is possible that such small defects should be considered defects inherent to the material rather than manufacturing defects.

References

1. T. A. Harris, Rolling Bearing Analysis, NY, John Wiley and Sons, 2001, p.4, 348–349, 621–624.

2. S. V Didziulis et al., *Lubrication*, NASA Space Mechanisms Handbook, R. L Fusaro, Editor. NASA/TP-1999-206988, 1999, p. 233.

3. H. M. Chan and M. P. Harmer, *Processing of Ceramics, Materials Science and Technology Vol 17B*. R. J. Brook, editor. Weinheim: VCH, 1996. p. 177–215.

4. J. Dusza and M. Steen, Fractography and fracture mechanics property assessment of advanced structural ceramics, *Inter Mater Rev 1999* **44**(5),165–216.

5. R. W. Rice, Ceramic Fracture Features, Observations, Mechanisms and Uses. Fractography of Ceramic and Metal Failures, ASTM Special Technical Publication 827. J. J. Mecholsky, editor. Philadelphia: ASTM, 1984. p.75.

6. A. K. Mukhopadhyay et al., Fractographic Study of Sintered Si_3N_4, Sialon and RBSN, *J Mater Sci Letters 1987* **6**, 1198–1200.

7. T. Kawakubo and Komeya K., Static and Cyclic Fatigue Behavior of a Sintered Silicon Nitride at Room Temperature, *J Am Cer Soc 1987*, **70**(6), 400–405.

8. C. J. Gilbert et al., Behavior of Cyclic Fatigue Cracks in Monolithic Silicon Nitride, *J Am Cer Soc 1995* **78** [9], 2291–2300.

9. J. J. Swab and G. D. Quinn, Fractography of Advanced Structural Ceramics: Results from Topic #2 of the VAMAS Round Robin Exercise, *Cer Eng Sci Proc 1995* **16**(7):929–938.

10 W. Park et al., Rolling Contact Fatigue and Load Capacity Tests of M62 Bearing Steel, *Proceedings of the 32nd Aerospace Mechanisms Symposium*, Cocoa Beach, 1998. S. W. Walker, editor. 1998. p.237–251.

11. W. Park et al., Microstructure, Fatigue Life and Load Capacity of PM Tool Steel REX20 for Bearing Applications, *Lub Eng 1999*, 20–30.

12. L. G. Johnson, *Theory and Technique of Variation Research*. NY: Elsevier, 1964.

13. G. Lunberg and A. Palmgren, Dynamic Capacity of Rolling Bearings. Ingenior Vetenskaps Akademiens (IVA) Handligar (Royal Swedish Academy of Engineering Sciences, Proceedings), NR 196, 1947, Stockholm.

14. G. Lunberg and A. Palmgren, Dynamic Capacity of Roller Bearings. IVA Handligar, NR 210, 1952.

15. W. Weibull, A Statistical Theory of the Strength of Materials. IVA Handligar, NR 151, 1939.

16. W. Weibull, The Phenomenon of Rupture in Solids. IVA Handligar, NR 153, 1939.

17. E. Y. Robinson, Stress Rupture Model for Design with Composite Materials. AIAA Paper No. 97-2723, 33rd AIAA/ASME/SAE/SAEE Joint Propulsion Conference, July 6–9, 1997, Seattle, WA.

18. J. Lieblein and M. Zellen, Statistical Investigation of the Fatigue Life of Deep-Groove Ball Bearings, *J Res Natl Bur Stand 1956*, **57**(5), pp 273–316.

19. T. Tallian, Weibull Distribution of Rolling Contact Fatigue Life and Deviations Therefrom, *ASLE Transactions 1962* **5**, 183–196.

20. S. J. Schneider, ed, *Engineered Materials Handbook, volume 4, Ceramics and Glasses*. Metals Park: ASM International. p.634.